Geodesy and Geodynamics 14 (2023) 231–243

Contents lists available at ScienceDirect

Geodesy and Geodynamics

journal homepage: http://www.keaipublishing.com/geog

Local geoid modeling in the central part of Java, Indonesia, using terrestrial-based gravity observations

Rahayu Lestari [a], Brian Bramanto [b, *], Kosasih Prijatna [b], Arisauna M. Pahlevi [c], Widy Putra [c], Raa Ina Sidrotul Muntaha [c], Febriananda Ladivanov [c]

[a] Departement of Geodesy and Geomatics Engineering, Faculty of Earth Sciences and Technology, Institut Teknologi Bandung, Indonesia
[b] Geodesy Research Group, Faculty of Earth Sciences and Technology, Institut Teknologi Bandung, Indonesia
[c] Geodetic and Geodynamic Control Network Center, Geospatial Information Agency of Indonesia (BIG), Indonesia

ARTICLE INFO

Article history:
Received 8 September 2022
Accepted 23 November 2022
Available online 22 December 2022

Keywords:
Gravimetric geoid
Stokes integration
Second Helmert's condensation method
GNSS/Leveling

ABSTRACT

The Global Navigation Satellite System (GNSS) positioning method has been significantly developed in geodetic surveying. However, the height obtained through GNSS observations is given in a geodetic height system that needs to be converted to orthometric height for engineering applications. Information on geoid height, which can be calculated using the global geopotential mode, is required to convert such GNSS observations into orthometric height. However, its accuracy is still insufficient for most engineering purposes. Therefore, a reliable geoid model is essential, especially in areas growing fast, e.g., the central part of Java, Indonesia. In this study, we modeled the local geoid model in the central part of Java, Indonesia, using terrestrial-based gravity observations. The Stokes' formula with the second Helmert's condensation method under the Remove-Compute-Restore approach was implemented to model the geoid. The comparison between our best-performing geoid model and GNSS/leveling observations showed that the standard deviation of the geoid height differences was estimated to be 4.4 cm. This geoid result outperformed the commonly adopted global model of EGM2008 with the estimated standard deviation of geoid height differences of 10.7 cm.

1. Introduction

The Global Navigation Satellite System (GNSS) is one of the positioning methods that has significantly developed in the last decades. Compared with other terrestrial positioning methods, e.g., positioning using a total station, GNSS is much more efficient, cost-effective, and accurate [1]. One can achieve up to a few millimeters of positioning accuracy when using GNSS precise positioning techniques, such as static differential positioning and precise point positioning [2–5]. Further, the real time kinematic (RTK) technique enables users to obtain several centimeters positioning accuracy instantaneously [6,7]. However, one of the drawbacks when using GNSS positioning is the height reference. GNSS uses height above the reference ellipsoid (referred to as geodetic height system), which is uncommon for engineering applications, e.g., mapping. On the other hand, most users demand accurate positions that are referenced to the mean sea level (MSL), which can be referred to as an orthometric height system. Consequently, the height obtained through GNSS observations needs to be converted to orthometric height for practical implementations [8].

The information on the height difference between the reference ellipsoid and MSL is needed to convert any point from GNSS observations. When the influence of, e.g., wind and tide are absent, the MSL has the same geopotential at all points on the surface [9–11]. This surface is also known as the geoid surface. The relationship between the Earth's surface, the reference ellipsoid, and the geoid surface at one point is shown in the following simple equation:

* Corresponding author.
E-mail address: brian.bramanto@itb.ac.id (B. Bramanto).
Peer review under responsibility of Institute of Seismology, China Earthquake Administration.

Production and Hosting by Elsevier on behalf of KeAi

https://doi.org/10.1016/j.geog.2022.11.007

$$H = h - N \quad (1)$$

where N is the geoid undulation or the height difference between the reference ellipsoid and geoid surface; h is the height above the reference ellipsoid (the geodetic height system) obtained from the GNSS measurement; and H is the height above the geoid surface (the orthometric height system). In addition, Fig. 1 displays the schematic relationship between geoid undulation, geodetic height system, and orthometric height system.

The conversion of geodetic height to orthometric height using geoid undulation is a straightforward method when the geoid undulation model is known with acceptable accuracy, i.e., millimeter to centimeter level, for precise engineering purposes. One of the geoid models that is commonly used to serve this application is the Earth Geopotential Model 2008 (EGM2008) [12]. The root mean square (RMS) differences between GNSS/leveling- and EGM2008-derived geoid height were estimated to be about 0.19 m based on 24014 validation points in Australia, Brazil, Canada, Europe, Japan, Mexico, and the USA (after the International Centre for Global Earth Models (ICGEM); http://icgem.gfz-potsdam.de/tom_gpslev, last accessed on August 22, 2022). In Egypt, Dawod et al. [13] also evaluated the performance of the EGM2008 geoid model and estimated the standard deviation of geoid height differences to be 0.23 m. Another similar study in South Korea also showed a similar result, with the standard deviation of geoid height differences estimated to be 0.19 m [14]. Unfortunately, the EGM2008 model's accuracy is still insufficient to comply with the needs of precise engineering applications.

In Indonesia, the demand for precise geoid models has been high for the last few years. Many infrastructure projects have been initiated in many areas. For example, in the Central Java and Daerah Istimewa Yogyakarta provinces, the Ministry of Public Works and Housing has built several infrastructures, including roads and bridges, water resource management, regional arrangement, and waste management sites [15]. In the near future, the Semarang - Demak (Semarak) Toll Road is also expected to be established. The toll road will be integrated with the Semarang City Sea Wall and is expected to support the growth of the new economic center in Central Java Province [16,17]. These infrastructure developments rely on precise topographical maps, which can be efficiently made using GNSS-based positioning with a precise geoid model. Therefore, there is a definite need for an accurate geoid model to obtain accurate conversions on the transformation from geodetic height to orthometric height to maximize infrastructure development in this region.

This study aims to obtain a reliable geoid model of the central part of Java, where the Central Java and Daerah Istimewa Yogyakarta provinces are located. The gravimetric geoid modeling approach was used to obtain the geoid model in this area. It incorporated the available terrestrial gravity observations in the vicinity of the target area. The model was further assessed by comparing the geoid height between the obtained model and the GNSS/leveling observations.

The remainder of this paper is structured as follows: section 2 describes data that is used in this study; section 3 briefly explains the method used to model the gravimetric geoid; section 4 shows the numerical results, validates the models with external data, and discusses the findings; and finally, section 5 summarizes the study and gives an outlook of future studies.

2. Data

Four primary data are needed to model the gravimetric geoid. They include gravity observations, the global geopotential model, the topography model, and fill-in gravity observations. Fig. 2 shows the distribution of the terrestrial and fill-in gravity observations.

2.1. Terrestrial gravity observations

The gravity was measured in 2019 by the Geospatial Information Agency of Indonesia (BIG) using the Scintrex CG-5 and CG-6 relative gravimeters. Both instruments are designed for high-precision gravity data acquisition, with an accuracy of greater than 5 μGal (1 μGal is equal to 10^{-8} ms^{-2}) [18,19], allowing us to use this instrument for a wide spectrum of applications [20–22]. The gravity is observed based on the reading of the quartz spring's displacement associated with the gravity variation. The Scintrex CG-5 and CG-6 can measure gravity with a range of about 8000 mGal (1 mGal is equal to 10^{-5} ms^{-2}), with a reading resolution of 1 μGal. In addition, the use of quartz springs ensures that readings are not affected by variations in the magnetic field.

The gravity was collected in two main cities. They are Yogyakarta and Semarang cities located in the southern and northern parts of the study area. The gravity was sampled at an interval spacing of about 5 km. The gravity was measured in a loop system starting and ending at the gravity reference points, in which absolute gravity values were measured using the ballistic-type gravimeter of A10 with an accuracy of better than 10 μGal [23,24]. The measurement for each loop lasted no longer than 9 h, with the average drift estimated to be about 11 μGal/day. The drift for each loop is shown in Fig. 3. We compiled 264 gravity points consisting of 143 and 118 measurements in Yogyakarta and Semarang, respectively. The position of each gravity point was determined using geodetic-grade GNSS instruments. The RTK technique was considered as it provides position with an accuracy of several centimeters. We tied our observations to the nearest continuous GNSS stations operated by BIG, which are located no longer than 10 km from the observation points. The data and corrections

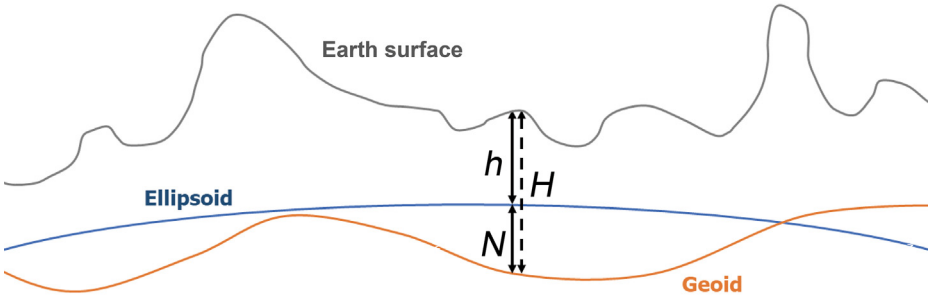

Fig. 1. The relationship between the ellipsoid, geoid, and the Earth's surface, where h is the geodetic height, N is the geoid height, and H is the orthometric height. The geoid undulation is positive when the geoid is above the reference ellipsoid and negative when the geoid is below the reference ellipsoid.

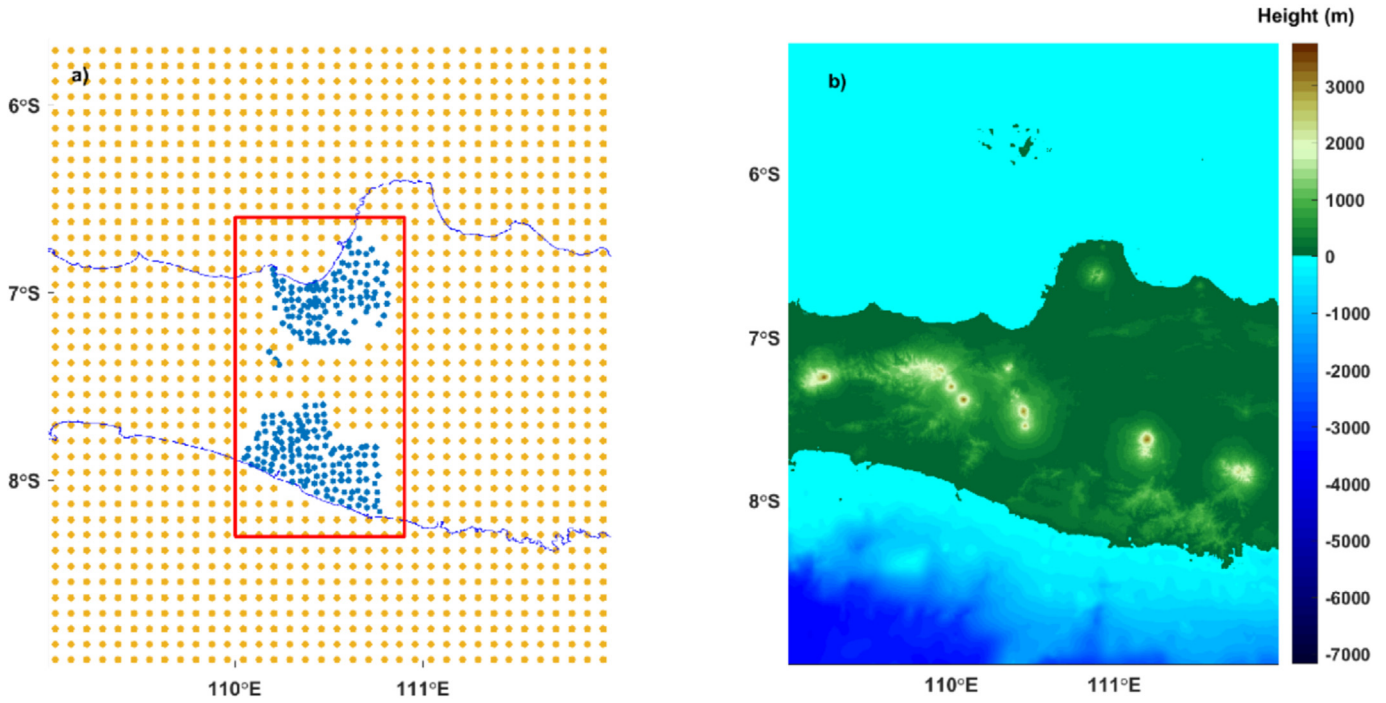

Fig. 2. The distribution of terrestrial (blue dots) and fill-in (orange dots) gravity observations. The red box indicates our target area, while the blue lines represent the coastlines. (b) The topography of the study area is based on a combination between SRTM.

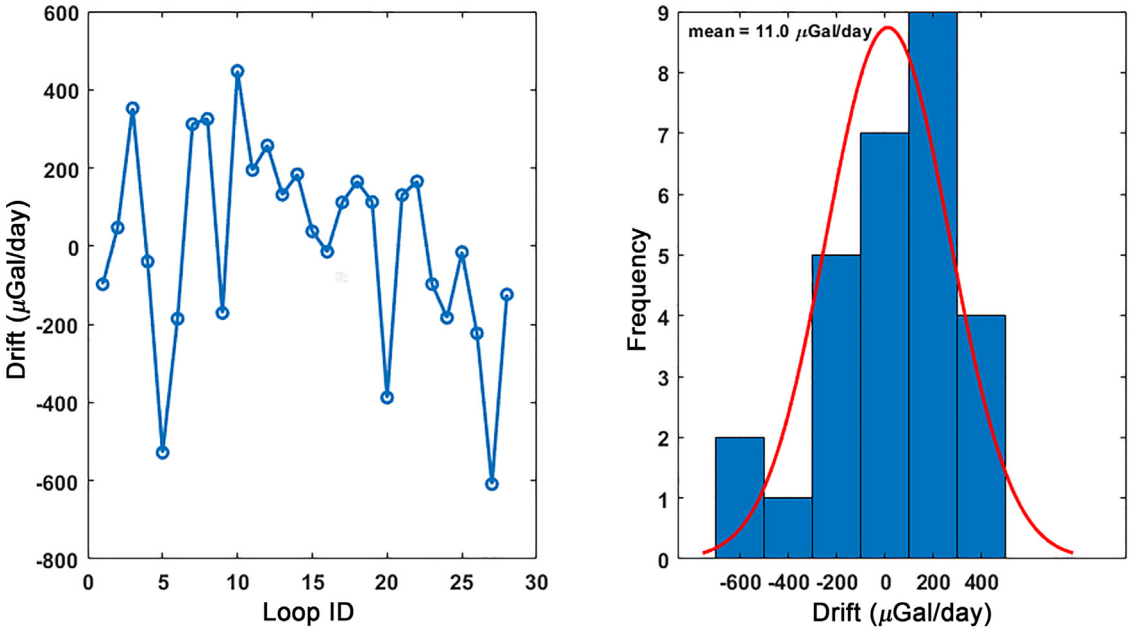

Fig. 3. The estimated drift for each loop (left panel) and the corresponding histogram plot (right panel). The red line represents the normal distribution fit.

between GNSS receivers were given instantaneously through the internet.

2.2. Global geopotential model (GGM)

The GGM in this study was used as the reference geoid and also to fill the gaps in gravity observations (described later). The spherical harmonic coefficients of GGMs are publicly listed on the ICGEM website (http://icgem.gfz-potsdam.de/ICGEM/) [25]. They can be downloaded for free with different accuracy and spatial resolution depending on the chosen model [26].

We tested several high-degree coefficients of GGMs to choose which GGMs suit our case most by comparing the modeled gravity anomaly with the observed gravity anomaly from the terrestrial gravity observations. The tested models were the Earth Geopotential Model 2008 (EGM2008 [12]), experimental gravity field model 2019e (XGM2019e [27]), and European Improved Gravity model of the Earth by New techniques-6C4 (EIGEN-6C4 [28]). All

of these models were evaluated with degree and order (d/o) of up to 2190, corresponding to a spatial resolution of about 10 km or about 5'.

Table 1 lists the statistic of gravity difference between the evaluated GGM and terrestrial gravity observations. The evaluation was made at difference d/o also to investigate its effects. The average gravity difference was generally increased as higher d/o was used, in which the positive mean values were observed for all cases. This indicates that GGM-derived gravity values were generally larger than the observed ones. Nevertheless, we observed that the range of gravity difference was also decreased with higher d/o. To choose which GGM is suited for our case, we considered looking for the smallest standard deviation of gravity difference. Based on the evaluation results, it was found that EGM2008, with a d/o of 2190, had the best performance (in terms of standard deviation) among other GGMs. EGM2008 with a d/o of 2190 had a standard deviation of 13.7 mGal. It was followed by EIGEN-6C4 (d/o 2190) with a standard deviation of 14.4 mGal. XGM2019e (d/o 2190) gave a poorer performance with a standard deviation of 16.6 mGal. Finally, EGM2008 was chosen for the concurrent analysis.

2.3. Topography data

The available high-resolution elevation model covering our study area is the Shuttle Radar Topography Mission (SRTM [29]) with a spatial resolution of 1 arc-second. However, this elevation model only covers the land area, while the elevation data over the ocean region remains empty. Recently, the SRTM15+ [30] has been released as the latest iteration of the SRTM+ elevation model, which also covers ocean bathymetry. The ocean region was derived from the sounding observation and satellite-derived bathymetry. The model is given with a sampling interval of 15 arc seconds. This study used a suit combination between SRTM 1 arc-second and SRTM15+ covering both land and ocean regions. Before combining these two models, the elevation data given with a spatial sampling interval of 15 arc seconds was first interpolated to the native spatial resolution of the SRTM model. The interpolated value replaced the data gaps in SRTM over the ocean area from SRTM15+.

We further evaluated the performance of the elevation model by comparing it with GNSS/leveling observation (described later) and gravity points. In total, we compiled more than 450 checkpoints in the vicinity of the study area. Table 2 lists the statistics of height differences at evaluation points. The height difference ranged between −33.819 and 32.728 m, with an average of 4.291 m. The standard deviation of height difference was estimated to be 4.761 m. It should be noted that the topography assessment was only made for the land area, while the accuracy of the topography model in the ocean region remains unclear.

Table 1
Statistic of gravity differences between GGM- and terrestrial-derived gravity observations for each evaluated GGM at different degrees and orders. The unit is in mGal.

Model	d/o	Minimum	Maximum	Mean	Standard deviation
EGM2008	360	−77.4	89.7	3	22.8
	720	−66.6	91.3	7.4	20.2
	1080	−44.5	84.9	9.9	16.9
	1440	−42.5	86.5	8.9	14.9
	1800	−45.5	90.6	9.3	14
	2160	−41.9	83.2	9.3	13.9
	2190	−41.7	82.8	9.3	13.7
EIGEN-6C4	360	−78.9	91.3	2.1	23.4
	720	−68.9	92.6	6.7	20.6
	1080	−46.9	86.1	9.2	17.5
	1440	−45.9	87.5	8.2	15.5
	1800	−48.9	91.5	8.6	14.7
	2160	−44.9	84.4	8.6	14.5
	2190	−43.9	84	8.6	14.4
XGM2019e	360	−79.9	91.1	3.4	22.9
	720	−67.9	91.9	9	20.7
	1080	−51.9	95.4	12.3	19.7
	1440	−45.9	96.9	11.3	17.6
	1800	−48.9	101.4	11.7	16.7
	2160	−42.9	91.7	11.8	16.6
	2190	−42.9	91.4	11.8	16.5

2.4. Fill-in gravity observations

The local geoid computation requires the regional integration of gravity observation that extends across the target area and its vicinity. Recalling our terrestrial-based gravity observations that only cover parts of our target area, the gaps in gravity observations in geoid modeling can lead to poor geoid model results.

To fill the data gaps over the land and sea regions, we synthesized gravity observations by following the methodology presented by Zaki et al. [31] called the spectral enhancement method. The basic principle of this method is to combine the long wavelength gravity component from the chosen GGM and the short wavelength gravity component from the terrain. The corresponding terrain gravity effects were calculated based on the so-called residual terrain model (RTM) proposed by Forsberg [32]. It forward-models the attraction effects of the differences between the higher and lower resolution of elevation models.

The fill-in gravity observations can be mathematically described as follows:

$$g_{\text{fill-in}} = g_{\text{GGM}} + g_{\text{RTM}} \tag{2}$$

where g_{GGM} is the gravity value from the chosen GGM, and g_{RTM} is the RTM gravity effects from the topographic reference model. In this study, we used the EGM2008 with d/o of up to 2190 as it gives the best performing GGM as indicated in section 2.2. As described in section 2.3, the combined elevation model was used as the higher-resolution elevation model. The lower-resolution elevation model was defined by smoothing the higher-resolution elevation model to be equivalent to a 5′ bin of spatial resolution, which follows the spatial resolution of EGM2008. The fill-in gravity observations cover the entire study area and extend to about 1° beyond the target area to minimize the edge effects [33].

3. Gravimetric geoid modeling

The gravimetric geoid modeling is more reliable than geometric geoid modeling (using GNSS/leveling) for modeling a high-resolution geoid model over a large or regional area. This is because gravity anomalies are relatively easy to measure over a large area without any cumulative errors that occur when using geometric-based observations (e.g., GNSS/leveling) to model the geoid [26]. One can model the geoid using the classical Stokes' formula as follows:

$$N = \frac{R}{4\pi\gamma}\int\int \Delta g S(\psi)\partial\sigma \tag{3}$$

Table 2
Statistic of height difference between the model and terrestrial observations at checkpoints. The unit is in meters.

Minimum	Maximum	Mean	Standard deviation
−33.819	32.728	4.291	4.761

where R is the mean radius of Earth; γ is the normal gravity on the reference ellipsoid; Δg is the gravity anomaly; $S(\psi)$ is the Stokes' function; and $\partial\sigma$ is the element of the surface.

Geoid undulation calculation using Stokes' formula shows that the numerical integration must be carried out for all spherical surfaces. However, the gravity measurements (e.g., using terrestrial- and airborne-based gravimeters) are generally limited to the study area. To overcome this problem in local or regional geoid modeling, the Remove-Compute-Restore (RCR) is one of the most applied approaches to be adopted [34–36]. First, RCR subtracts both long (predicted by GGM) and short-wavelength (predicted by topography model) gravity components from the gravity observations. The residual part is then computed by using Stokes' integration methods. Finally, the long and short-wavelength components of the geoid are restored, obtaining a complete wavelength of the geoid model. As indicated, the RCR technique focuses on the residual part to simplify the computation [11].

Another note when using Stokes' formula is to remove all topographic masses outside the geoid to a layer on or below the geoid [37]. Therefore, the observed gravity on or above the Earth's surface should be reduced to the geoid surface. Helmert's second condensation method is one of the common methods to be adopted, in which the gravitational attraction of the topographical masses above the geoid is condensed onto a layer on the geoid [38].

To simplify, we refer above methods as Stokes-Helmert's method. The following are the procedures to compute the geoid using Stokes-Helmert's method when using terrestrial gravity observations.

1. The calculation begins by first reducing the observed gravity obtained from terrestrial gravity measurements from the Earth's surface to the geoid and constructing the free-air gravity anomaly. This shows that all the topographical mass above the geoid is condensed into a geoid according to Helmert's 2nd condensation method. The observed gravity is reduced to the geoid surface using a free-air gravity gradient to obtain the free-air gravity anomaly. Mathematically, the free-air gravity anomaly can be described as follows [39]:

$$\Delta g_{\mathrm{fa}} = g_{\mathrm{obs}} - \gamma + \delta g_{\mathrm{fc}} + \delta g_{\mathrm{atm}} \tag{4}$$

where g_{obs} is the observed gravity from terrestrial and fill-in gravity measurements, δg_{fc} is the free-air correction, and δg_{atm} is the atmospheric correction.

2. Next, the free-air gravity anomaly is smoothed by converting it to Bouguer gravity anomaly using the simple planar Bouguer reduction. Bouguer reduction removes the effect of gravity from all masses (assuming constant density) above the geoid surface from the observed gravity [40]. To determine the free-air gravity anomaly from the Bouguer anomaly, follow the equation [41]:

$$\Delta g_{\mathrm{B}} = \Delta g_{\mathrm{fa}} - 2\pi \mathrm{G}\rho H_p \tag{5}$$

where G is the gravitational constant; ρ is the density value; and H_p is the topographic height at the observation points. For land areas, the density is set to be 2670 kg/m^3 while 1686 kg/m^3 is the density value for the ocean areas. The density value for the ocean areas is the difference between rock and seawater densities.

3. Remove the long-wavelength gravity component from the observation using the chosen GGM. In this study, we used EGM2008 to remove the corresponding gravity component.

4. Add the terrain correction. The terrain correction is determined from the irregular terrain after removing the effects of planar Bouguer gravity and is formulated as follows:

$$T_c = \mathrm{G}\rho \iint_{-\infty}^{\infty} \int_{z_p}^{z} \frac{z - z_p}{\sqrt{(x - x_p)^2 + \left(y - y_p\right)^2 + (z - z_p)^2}} \partial x \partial y \partial z \tag{6}$$

where x, y, z are the planar coordinates of the discretized irregular terrain, and x_p, y_p, z_p indicate the coordinate of the computation point.

5. Remove the indirect gravity effects from the data due to the removal of Helmert's topographic mass. The effect can be estimated as follows:

$$\delta\Delta g = \left(\frac{2\pi \mathrm{G}\rho}{R}\right) H_p^2 \tag{7}$$

6. Grid the residual reduced gravity anomaly as obtained from steps 2–5 that is given by:

$$\Delta g_{\mathrm{red}} = \Delta g_{\mathrm{B}} + T_c - \Delta g_{\mathrm{GGM}} + \delta\Delta g \tag{8}$$

Several methods can be used to grid the residual reduced gravity anomaly, e.g., by using kriging interpolation or least-squares prediction approaches [42], at the desired spatial resolution ($\Delta g_{\mathrm{red}}^{\mathrm{grid}}$).

7. Restore the Bouguer gravity effect to produce the residual Faye gravity anomaly:

$$\Delta g_{\mathrm{Faye}} = \Delta g_{\mathrm{B}} + B + T_c - \Delta g_{\mathrm{GGM}} + \delta\Delta g \tag{9}$$

In this study, the reduced gravity anomaly had been gridded. Therefore, the calculation of the gridded residual Faye gravity anomalies follows:

$$\Delta g_{\mathrm{Faye}}^{\mathrm{grid}} = \Delta g_{\mathrm{red}}^{\mathrm{grid}} + B_{\mathrm{grid}} \tag{10}$$

where B_{grid} is the planar Bouguer gravity effect at the corresponding grid points.

8. Compute the residual geoid undulation as in Eq. (3), using the gridded residual gravity anomalies $\Delta g_{\mathrm{Faye}}^{\mathrm{grid}}$. We implemented the Fast Fourier Transform (FFT) technique to evaluate the numerical integration. Assuming the planar approximation of Stokes' formula, Eq. (3) can be written as [43]:

$$N_{\mathrm{res}}^{\mathrm{grid}} = \frac{1}{2\pi\gamma} \iint \frac{\Delta g_{\mathrm{Faye}}}{\sqrt{(x_p - x)^2 + \left(y_p - y\right)^2}} \partial x \partial y \tag{11}$$

9. Compute the geoid undulation at the corresponding grid points from the GGM to restore the long-wavelength component of the geoid. When using the spherical harmonic coefficients of GGM, the geoid can be calculated as [10]:

$$N_{\mathrm{GGM}}^{\mathrm{grid}} = R \sum_{n=2}^{M} \sum_{m=0}^{n} \left[C_{nm} \cos m\lambda_p + S_{nm} \sin m\lambda_p\right] P_{nm}\left(\sin\phi_p\right) \tag{12}$$

where C_{nm} and S_{nm} are the fully normalized spherical harmonic coefficients, given degree n and order m; $P_{nm}(\sin\phi_p)$ is the fully normalized associated Legendre functions; M is the maximum degree of GGM; λ and ϕ are the respective longitude and latitude coordinate of the computation point p.

10. Restore the indirect geoid effects at the corresponding grid points due to the Helmert's condensed masses that can be calculated as follows:

$$\delta N^{\text{grid}} = -\frac{\pi\mu}{\gamma}H^2 - \frac{\mu}{6\gamma}\iint\frac{H^3 - H_p^3}{(H - H_p)^3}\partial x\partial y \tag{13}$$

with $\mu = G\rho$.

11.Finally, assemble the Stokes-Helmert's geoid by adding all of the geoid components from the previous steps as:

$$N_H^{RCR} = N_{GGM}^{\text{grid}} + N_{\text{res}}^{\text{grid}} + \delta N^{\text{grid}} \tag{14}$$

4. Results and discussion

4.1. Geoid results

Two geoid models with different resolutions, i.e., the 5′ and 1′ resolution geoid models, were modeled through this study. The 5′ resolution was chosen following the resolution of the EGM2008 with degrees and order 2190, which has a spatial resolution of roughly about 5'. On the other hand, the 1′ resolution was chosen to comply with the sampling interval of the terrestrial gravity observations of about 5 km (approximately 1′). These two scenarios of the geoid model were performed to evaluate the effect of the model's resolution on the accuracy and precision of the resulting geoid models.

Fig. 4 shows the geoid for each component as mentioned on the right-hand side of Eq. (14) for the 5′ and 1′ bins. The long-wavelength components ranged from about 0 to about 35 m, while the terrain's indirect geoid effects contributed from about −0.5 to about 0 m. The residual geoid components ranged from about −0.3 to about 0.2 m, with the lowest geoid values located in Semarang city. On the other hand, the high geoid values in residual components were mostly observed in areas with a significant topography, e.g., mountainous areas.

Fig. 5a and 5b show the respective geoid model for the 5′ and 1′ resolutions using Stokes-Helmert's method. The 5′ geoid model ranged from 0.964 to 31.634 m. While for the 1′ geoid model, it ranged from 0.978 to 31.799 m. Visually, the 1′ geoid model had a smoother surface as it has a higher resolution than the 5′ geoid model and did not differ significantly. We then subtracted these models from each other to obtain the geoid difference as depicted in Fig. 5c. The difference in geoid undulation between these two geoid models with different resolutions was estimated to be about ±20 cm.

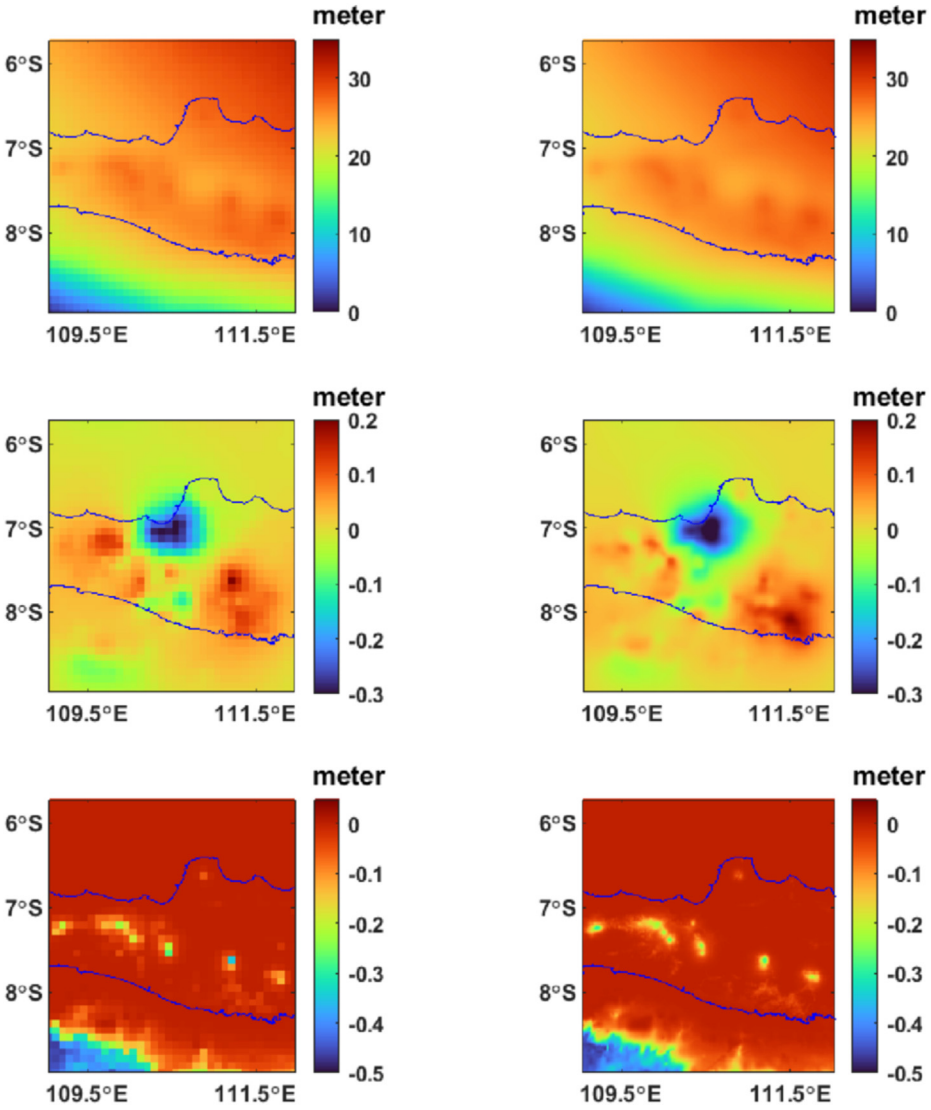

Fig. 4. The resulting geoid for each component. The upper panels show the long-wavelength geoid components from the chosen GGM. The middle and lower panels display the residual and indirect geoid components, respectively. The left and right panels display the corresponding components when we set the spatial resolution to be 5′ and 1′, respectively.

The significant discrepancies were mostly observed in mountainous areas and depth ocean bathymetry (southwest of the study area).

4.2. Validation with GNSS/leveling data

We further investigated the performance of our geoid models by comparing them with the geoid as observed using the GNSS/leveling method. The geoid at the measurement points is obtained by subtracting the ellipsoid heights with the orthometric heights observed using GNSS and leveling approaches, respectively. When the gravity is also observed at the measurement points, the non-parallel equipotential surface can be corrected [10,44]. However, the leveling measurements used in this study were not corrected from such matter.

We compiled 197 GNSS/leveling points that extend north to south from Semarang to Yogyakarta. GNSS observations were carried out using the static differential positioning method and tied to at least two continuous GNSS stations available in the vicinity of the study area. The observations were made using geodetic-grade GNSS instruments, while the observations lasted for 36 h at each measurement point. The leveling measurements were performed using a digital waterpass. The leveling was tied to the tidal benchmark in Yogyakarta. The difference of height difference between forward and backward levelings was less than 8 $\sqrt{K}$ mm, where K is the distance of the leveling measurements. Fig. 6 shows the distribution of GNSS/leveling points and the corresponding geoid values. The distance between GNSS/leveling points is about 10 km. The GNSS/leveling-derived geoid ranged from 24.597 to 26.877 m.

Figure 7 shows the comparison between gravimetric and GNSS/leveling geoid at the corresponding validation points, while Table 3 lists the overall statistics of the geoid height differences. The standard deviation of the geoid differences was estimated to be 0.170 m for the 5′ geoid model. The 1′ geoid model indicated a slightly better performance than the 5′ geoid model, with an estimated standard deviation of 0.162 m. We further noted that both geoid models show a significant mean bias of −0.597 and −0.611 m for the 5′ and 1′ geoid models, respectively.

The bias is possibly caused due to the zero-degree term to the geoid height with respect to the reference ellipsoid. We further investigate the zero-degree term by using the GNSS/leveling and GGM as follows [10]:

$$N_0 = \frac{GM - GM_0}{R\overline{\gamma}} - \frac{W_0 - U_0}{\overline{\gamma}} \tag{15}$$

where GM_0 and U_0 are the geocentric gravitational constant and the normal potential value of the reference ellipsoid, respectively; $\overline{\gamma}$ is the mean normal gravity value at the GNSS/leveling points as predicted using the chosen GGM; GM is the associated gravitational constant from GGM, and W_0 is the geopotential value of the global

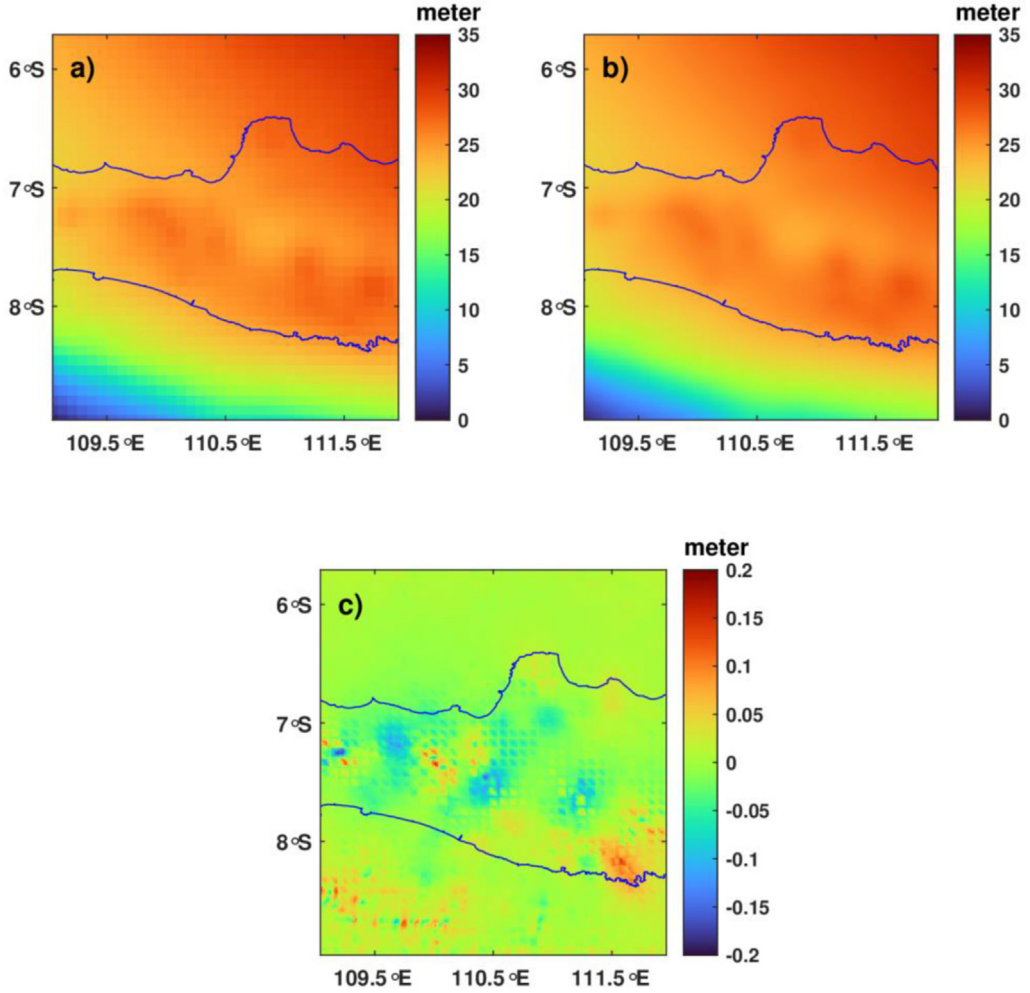

Fig. 5. The gravimetric geoid models with a spatial resolution of (a) 5′ and (b) 1'. (c) displays the differences between (a) and (b). The 5′ geoid model was first resampled to 1′ resolution before computing the difference between the 5′ and 1′ geoid models.

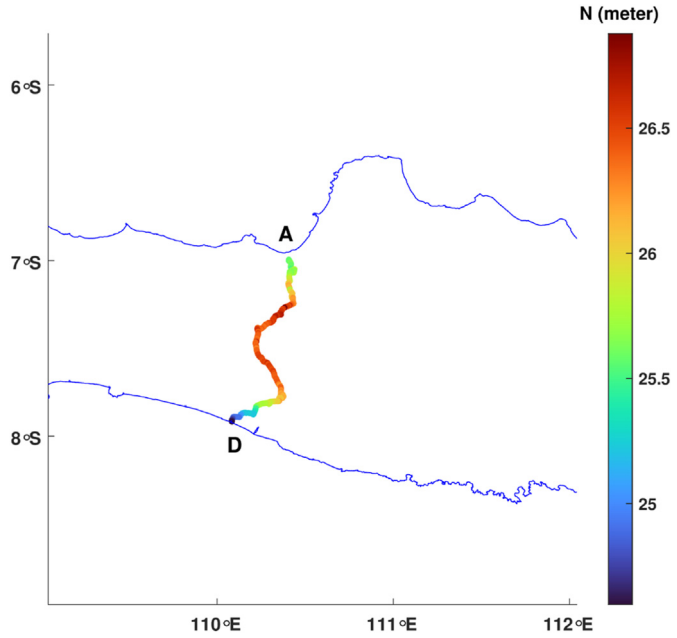

Fig. 6. GNSS/leveling data distribution in the central part of Java Island extends from north to south (A–D). Blue lines represent the coastlines.

vertical datum, which can be replaced by the value that is introduced by the International Union of Geodesy and Geophysics (IUGG) General Assembly in 2015.

The zero-degree term was estimated to be −0.442 m, which is only about two-thirds of the estimated bias. The remaining discrepancy is likely caused by the systematical error of gravity difference between the GGM and terrestrial-based gravity observations as indicated in Table 1, which shows that the terrestrial gravity observations were generally smaller than GGM. We further considered removing the bias observed in both geoid models using the corresponding mean bias. The bias-free geoid model ($N_{\text{bias-free}}$) is defined as follows:

$$N_{\text{bias-free}} = N_{\text{H}}^{\text{RCR}} - \frac{1}{n}\sum_{i=1}^{n}\left(N_{\text{H}}^{\text{RCR}}i - N_{vi}\right) \tag{16}$$

where N_v is the geometric geoid at GNSS/leveling point (i), and n is the number of GNSS/leveling points.

Table 3
Statistic of geoid height difference between gravimetric and GNSS/leveling geoid at the validation points. The unit is in meter.

Geoid model	Minimum	Maximum	Mean	Standard deviation
5′	−1.167	−0.275	−0.597	0.17
1′	−1.134	−0.289	−0.611	0.162

4.3. The effect of terrestrial gravity distribution on the geoid

As described previously, the terrestrial gravity observations were only distributed in the Semarang and Yogyakarta cities. We further divided the area of investigation into three parts (Semarang, Central, and Yogyakarta), as seen in Fig. 8, representing the differences in data distribution. We again investigated the geoid height difference between gravimetric and GNSS/leveling geoid at the validation points for each part.

Figure 9 displays the comparison of geoid height between gravimetric and GNSS/leveling at those three parts, while Table 4 lists the statistics of geoid height difference. The Yogyakarta part gave the best performance with the estimated standard deviation of 0.070 and 0.072 m for the 5′ and 1′ geoid models, respectively. It was followed by the Semarang part with an estimated standard deviation of 0.090 and 0.092 m for the 5′ and 1′ geoid models,

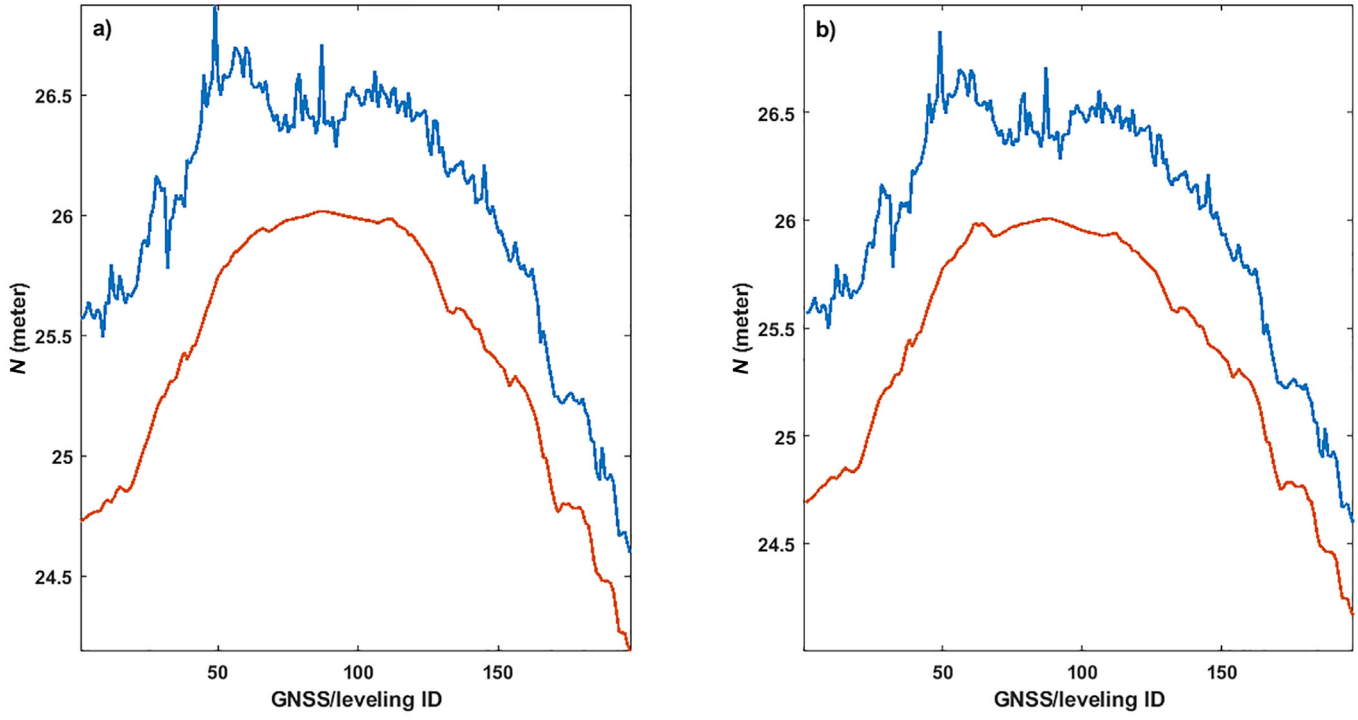

Fig. 7. The comparison between gravimetric (red lines) and GNSS/leveling (blue line) geoid at the corresponding validation points for (a) 5′ and (b) 1′ geoid models.

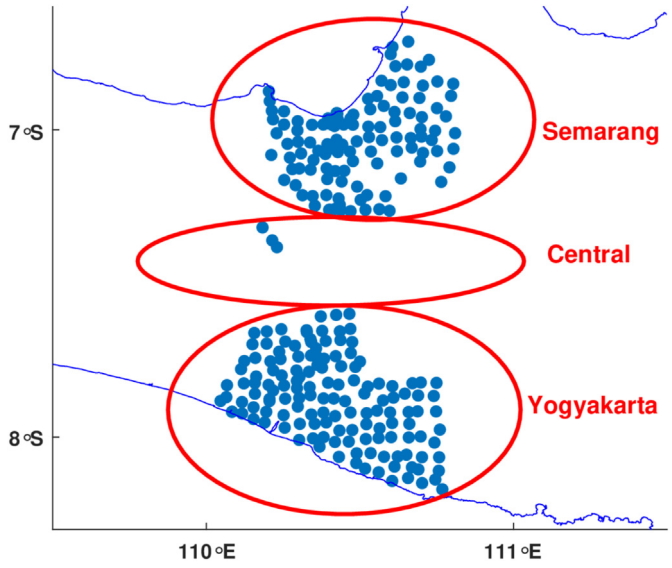

Fig. 8. Three divided parts for further investigation represent the differences in data distribution. Blue dots denote the terrestrial gravity measurements.

respectively. However, the standard deviation values were double for the Central part in both geoid models. This indicates that the lack of terrestrial gravity observations affects the accuracy of the resulting geoid model. In addition, the high-frequency component due to the relatively rough terrain in the Central part that was not observed by the terrestrial gravity observation may also contribute to the inaccurate geoid model in the Central part.

4.4. Final geoid model

The geoid models were further fitted to the GNSS/leveling observations. The GNSS/leveling observations were divided into two parts. The first part was used to obtain the correction surfaces, while the second part was used to validate the fitted geoid models. The odd-numbered points along the GNSS/leveling profile were used for fitting, while the even-numbered points were used for validation.

We tested three methods to fit our geoid models by modeling the differences between gravimetric geoid models and GNSS/leveling fitting points obtaining the surface correctors. The three methods were first-order polynomial regression, second-order polynomial regression, and kriging methods. The fitted geoid and GNSS/leveling observations are compared in Fig. 10. Visually, the geoid models that were fitted using the kriging method seem to

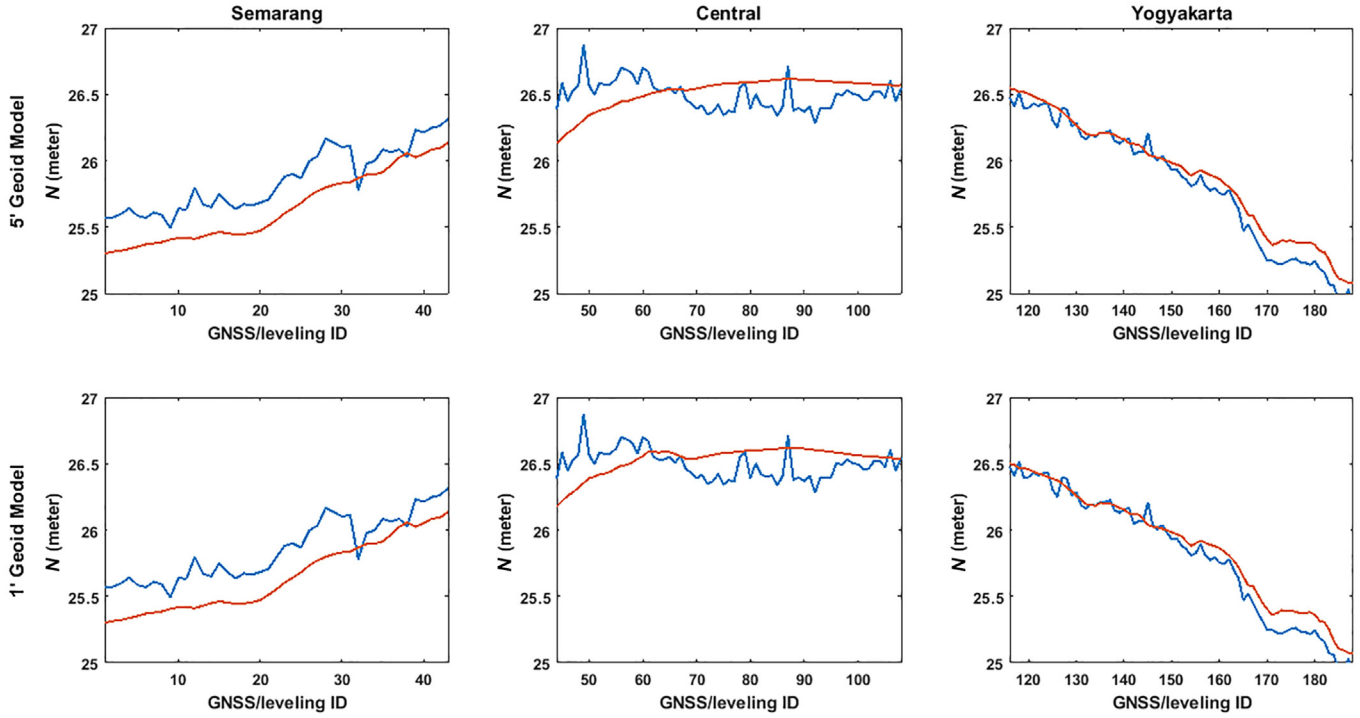

Fig. 9. The comparison between gravimetric (red lines) and GNSS/leveling (blue line) geoid for each part. The left, middle, and right panels represent the Semarang, Central, and Yogyakarta parts, respectively. The upper and lower panels show the corresponding comparison for 5′ and 1′ geoid models, respectively.

Table 4
Statistics of geoid height difference between gravimetric and GNSS/leveling geoid at the validation points for each part. The unit is in meter.

Geoid model	Part	Minimum	Maximum	Mean	Standard deviation
5′	Semarang	−0.391	0.099	−0.209	0.089
	Central	−0.57	0.322	0.021	0.192
	Yogyakarta	−0.165	0.2	0.075	0.07
1′	Semarang	−0.385	0.089	−0.207	0.091
	Central	−0.523	0.322	0.036	0.173
	Yogyakarta	−0.173	0.194	0.064	0.072

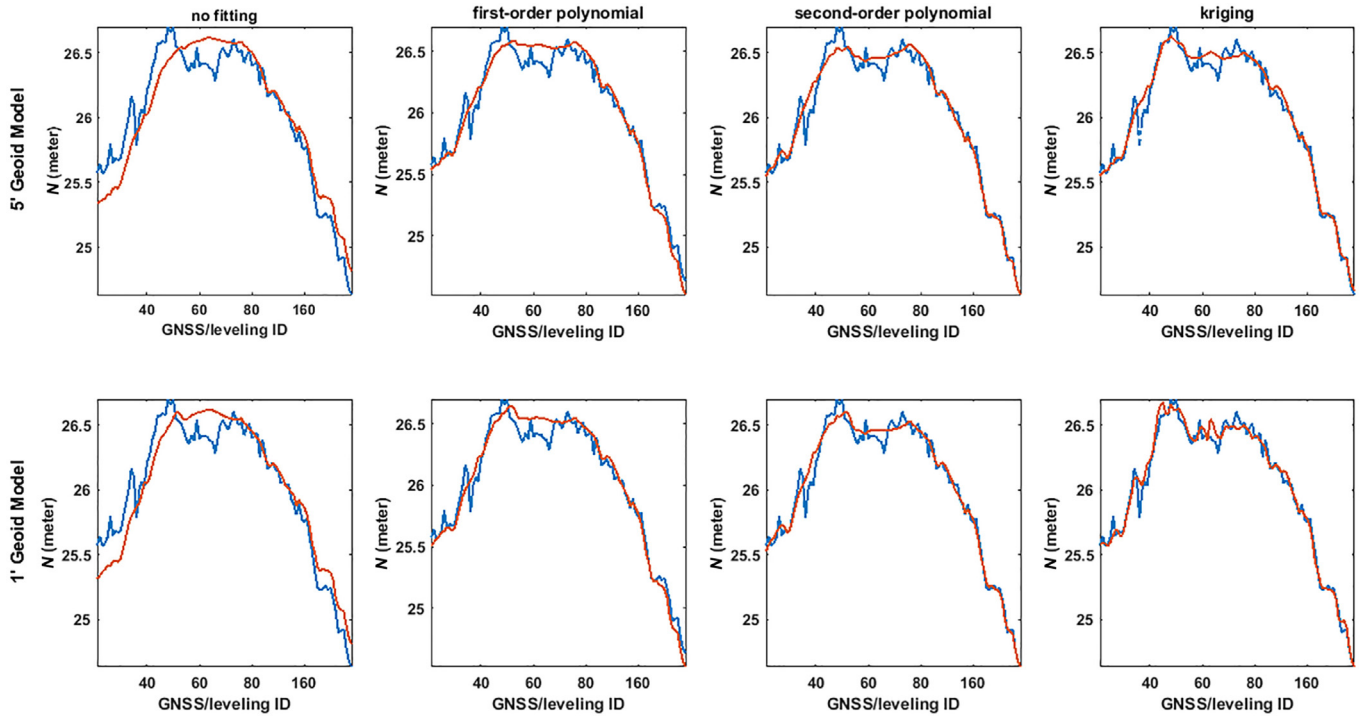

Fig. 10. The comparison between gravimetric (red lines) and GNSS/leveling (blue line) geoid for each fitting method. The first columns represent the uncorrected geoid comparison. The second, third, and fourth columns compare the first-order polynomial, second-order polynomial, and kriging methods to fit the gravimetric geoid models to GNSS/leveling observations. The upper and lower panels show the respective model with 5′ and 1′ spatial resolution, respectively.

better suit the GNSS/leveling observations than the other fitting methods, especially in the middle section.

We further computed the statistics of geoid height differences between the fitted geoid and GNSS/leveling observations for each method to verify the results (Table 5). The fitted geoid models using the kriging method had the smallest standard deviation of geoid height differences of 0.072 and 0.044 m for the 5′ and 1′ fitted geoid models, respectively. The second-order polynomial regression method gave the second-best performance with the estimated standard deviation of geoid height differences of 0.087 and 0.079 m for the 5′ and 1′ fitted geoid models, respectively. The first-order polynomial regression method failed to provide the sub-decimeters geoid accuracy for the 5′ geoid model with an estimated standard deviation of 0.102 m. While for the 1′ geoid model, the standard deviation was estimated to be 0.095 m.

The superior of the kriging method to fit the geoid model is also shown by the variability of the corrector surface (Fig. 11). The kriging method only corrected the geoid surface in the vicinity of the fitting points with a magnitude of about ±0.25 m. However, this is not the case when using the first and second-order polynomial methods to fit our geoid models. The corrector extended to the area that was far from the fitting points. The correction ranged from −2 to 1.5 m when using the first-order polynomial method. Its variability increased significantly to ±5 m when using the second-order polynomial method. This indicates that the method to fit the geoid model to the GNSS/leveling observations must be done carefully, especially when validation points are not distributed equally for all regions. Selecting the wrong method to fit the geoid may significantly affect the resulting geoid models.

Finally, we compared the results with the performance of the EGM2008 model as the most commonly adopted model. The standard deviation of geoid height differences between EGM2008 and GNSS/leveling observations was estimated to be 0.107 m. Regarding the standard deviation of geoid height differences, the kriging-fitted geoid model with the spatial resolution of 1′ is about 2.5 times better than the EGM2008. The kriging-fitted geoid model

Table 5
Statistics of geoid height differences between the fitted geoid and GNSS/leveling observations for each fitting method. The unit is in meter.

Geoid model	Fitting method	Minimum	Maximum	Mean	Standard deviation
5′	no fitting	−0.57	0.273	0.000	0.170
	first-order polynomial	−0.44	0.214	0.000	0.102
	second-order polynomial	−0.429	0.161	0.000	0.087
	kriging	−0.342	0.160	0.000	0.072
1′	no fitting	−0.523	0.276	0.000	0.162
	first-order polynomial	−0.400	0.212	0.000	0.095
	second-order polynomial	−0.393	0.169	0.000	0.079
	kriging	−0.195	0.118	0.000	0.044

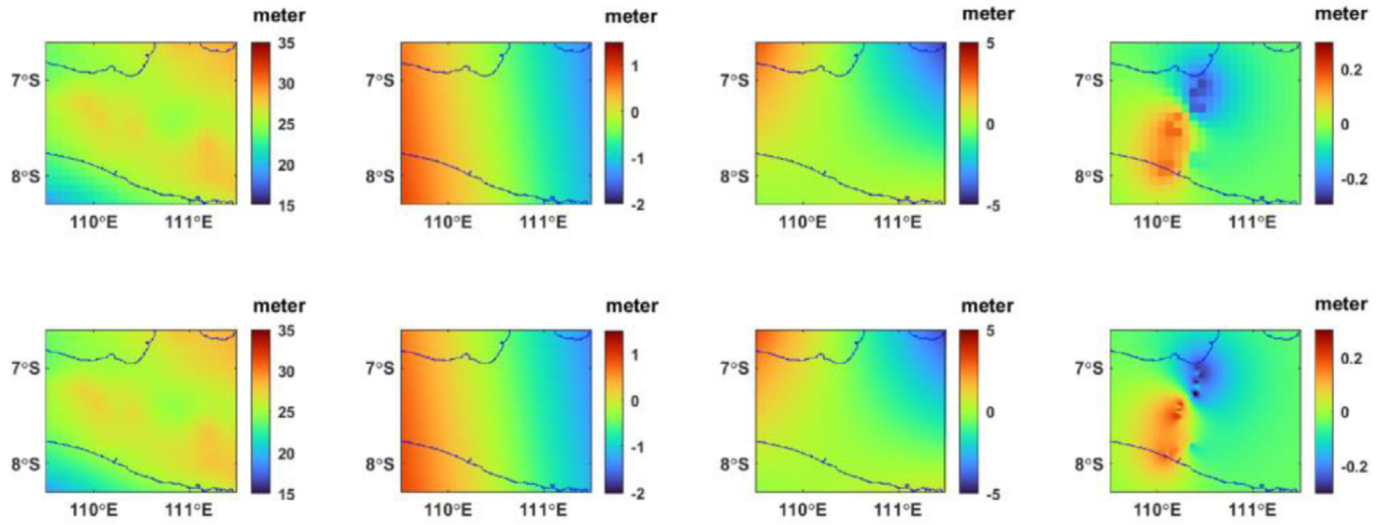

Fig. 11. The uncorrected geoid models (first column) and the corresponding surface correctors when using the first-order polynomial (second column), second-order polynomial (third column), and kriging method (fourth column). The upper and lower panels show the respective model with 5′ and 1′ spatial resolution, respectively.

with the spatial resolution of 5′ also performs better than the EGM2008.

5. Conclusion

We have computed the gravimetric geoid models of the central part in Java, Indonesia, using Stokes-Helmert's method with a spatial resolution of 1 and 5 min. The resulting geoid models contribute from short-wavelength (topography), long-wavelength (GGM), and residual components, in which the terrestrial gravity observations are used as the primary input for gravimetric geoid modeling in this study. In addition to the terrestrial gravity observations, we used the EGM for the chosen GGM and a suit combination of the SRTM 1 arc-second and SRTM15+ representing the respective land topography and ocean bathymetry. We further fit our geoid models to half of our GNSS/leveling observations using three methods, i.e., the first-order polynomial, second-order polynomial, and kriging methods.

Based on the validation with remaining GNSS/leveling observations, the fitted geoid results show that the kriging method performs better than other methods. Also, the higher geoid resolution helps to obtain the best geoid modeling performance. The standard deviation of the geoid height difference is estimated to be 4.4 cm for the 1′ fitted geoid model. While for the 5′ fitted geoid model, the corresponding standard deviation is estimated to be 7.2 cm. These results show the improvement in geoid performance compared with the direct use of EGM2008 to calculate the geoid in the vicinity of the study area, in which the standard deviation of the geoid height difference is estimated to be 10.7 cm.

We highlight that the primary data inputs are critical in precise gravimetric geoid modeling. The distribution of gravity observation should be intensified, especially in areas with very limited gravity observations. We also note a possible systematic bias in gravity between GGM and terrestrial gravity observations that need to be investigated further. Finally, the existing GNSS/leveling points are limited to one profile line and are not corrected for non-parallel equipotential surfaces. More GNSS/leveling observations with co-located gravity observations can improve the reliability of the validation and fitting of the geoid model. Nevertheless, we have shown that the resulting geoid models in this study outperform the commonly adopted global model of EGM2008.

Author contributions

Rahayu Lestari: investigation, software, formal analysis, writing – original draft, writing – review/editing, visualization. Brian Bramanto: conceptualization, methodology, software, formal analysis, investigation, writing – review/editing, supervision. Kosasih Prijanta: formal analysis, supervision, writing – review/editing. Arisauna M. Pahlevi: data curation, resources, writing – review/editing. Widy Putra: data curation, resources. Raa Ina Sidrotul Muntaha: data curation, resources. Febriananda Ladivanov: data curation, resources.

Conflicts of interest

The authors declare that there is no conflict of interest.

References

[1] F.H. Abdulrahman, Determination of the local geoid model in duhok region, university of duhok campus as a case study, Ain Shams Eng. J. 12 (2) (2021) 1293–1304, https://doi.org/10.1016/j.asej.2020.10.004.
[2] Y. Gao, Precise point positioning (PPP), in: Encyclopedia of Geodesy, Springer International Publishing, Cham, 2015, pp. 1–5.
[3] S.O. Eteje, O.F. Oduyebo, Comparative analysis of static differential GPS/GNSS positioning using two and three or more receivers, J. Environ. Earth Sci. 8 (12) (2018) 42–51, https://doi.org/10.5281/zenodo.2529968.
[4] S. Cetin, C. Aydin, U. Dogan, Comparing GPS positioning errors derived from GAMIT/GLOBK and Bernese GNSS software Comparing GPS positioning errors derived from GAMIT/GLOBK and Bernese GNSS software packages: a case study in CORS-TR in Turkey, Surv. Rev. 51 (2019) 369, https://doi.org/10.1080/00396265.2018.1505349.
[5] S. Lahtinen, et al., First results of the Nordic and Baltic GNSS analysis centre, J. Geod. Sci. 8 (1) (2018) 34–42, https://doi.org/10.1515/jogs-2018-0005.
[6] A.M. Manzino, P. Dabove, N. Gogoi, Assessment of positioning performances in Italy from GPS, BDS and GLONASS constellations, Geod Geodyn 9 (6) (2018) 439–448, https://doi.org/10.1016/j.geog.2018.06.009.
[7] I. Gumilar, B. Bramanto, F.F. Rahman, I.M.D.A. Hermawan, Variability and performance of short to long-range single baseline RTK GNSS positioning in Indonesia, E3S Web Conf. 94 (2019), 01012.
[8] A. Pirti, R.G. Hosbas, Evaluation of some levelling techniques in surveying application, Geod. Cartogr. 68 (2) (2019) 361–373, https://doi.org/10.24425/gac.2019.128463.
[9] L. Sanchez, et al., A conventional value for the geoid reference potential $$W_{0}$$ W 0, J. Geodes. 90 (9) (Sep. 2016) 815–835, https://doi.org/10.1007/s00190-016-0913-x.
[10] W.A. Heiskanen, H. Moritz, Physical Geodesy, Freeman, San Francisco, 1967.
[11] B. Hofmann-Wellenhof, H. Moritz, Physical Geodesy, Springer, Vienna, 2005.
[12] N.K. Pavlis, S.A. Holmes, S.C. Kenyon, J.K. Factor, The development and evaluation of the Earth gravitational model 2008 (EGM2008), J. Geophys. Res. 117 (B04406) (2012) 1–38, https://doi.org/10.1029/2011JB008916.

[13] G.M. Dawod, H.F. Mohamed, S.S. Ismail, Evaluation and adaptation of the EGM2008 geopotential model along the northern nile valley, Egypt: case study, J. Survey Eng. 136 (1) (2010) 36–40, https://doi.org/10.1061/(asce)su.1943-5428.0000002.
[14] K.B. Kim, H.S. Yun, H.J. Choi, Accuracy evaluation of geoid heights in the national control points of South Korea using high-degree geopotential model, Appl. Sci. 10 (4) (2020), https://doi.org/10.3390/app10041466.
[15] Pupr, A Closer Look at PUPR Infrastructure Development in Central Java (In Bahasa), 2021. Accessed: Sep. 04, 2022. [Online]. Available: https://www.pu.go.id/berita/melihat-lebih-dekat-pembangunan-infrastruktur-pupr-di-jawa-tengah.
[16] Pemerintah Provinsi Jawa Tengah, Proyek Tol Semarang-Demak Seksi II Ditarget Selesai 28 Oktober 2022, 2021. Accessed: Sep. 04, 2022. [Online]. Available: https://jatengprov.go.id/publik/proyek-tol-semarang-demak-seksi-ii-ditarget-selesai-28-oktober-2022/.
[17] Bpjt, Semarang - Demak Toll Road Development Continues to Protect Mangrove Areas on the Coastal Pantura, 2021. Accessed: Sep. 04, 2022. [Online]. Available: https://bpjt.pu.go.id/berita/semarang-demak-toll-road-development-continues-to-protect-mangrove-areas-on-the-coastal-pantura.
[18] Scintrex, Cg-5 Operation Manual, 2012.
[19] Scintrex, CG-6 Autograv Gravity Meter Operation Manual, 2018.
[20] F.J. Martinez-Moreno, J. Galindo-Zaldivar, A. Pedrera, T. Teixido, J.A. Pena, L. Gonzalez-Castillo, Regional and residual anomaly separation in microgravity maps for cave detection: the case study of Gruta de las Maravillas (SW Spain), J. Appl. Geophys. 114 (2015) 1–11, https://doi.org/10.1016/j.jappgeo.2015.01.001.
[21] D. Boddice, P. Atkins, A. Rodgers, N. Metje, Y. Goncharenko, D. Chapman, A novel approach to reduce environmental noise in microgravity measurements using a Scintrex CG5, J. Appl. Geophys. 152 (2018) 221–235, https://doi.org/10.1016/j.jappgeo.2018.03.022.
[22] O. Francis, Performance assessment of the relative gravimeter Scintrex CG-6, J. Geodes. 95 (10) (2021) 1–14, https://doi.org/10.1007/s00190-021-01572-y.
[23] J. Krynski, P. Dykowski, M. Sekowski, J. Makinen, On the estimate of accuracy and reliability of the A10 absolute gravimeter free-fall gravimeter, in: C. Rizos, P. Willis (Eds.), Earth on the Edge: Science for a Sustainable Planet, Springe, Berlin, Heidelberg, 2014, pp. 297–302.
[24] Micro-g LaCoste, A-10 Portable Gravimeter User's Manual, 2008.
[25] E. Sinem Ince, et al., Icgem – 15 years of successful collection and distribution of global gravitational models, associated services, and future plans, Earth Syst. Sci. Data 11 (2019) 647–674, https://doi.org/10.5194/essd-11-647-2019.
[26] K. Matsuo, Y. Kuroishi, Refinement of a gravimetric geoid model for Japan using GOCE and an updated regional gravity field model, Earth Planets Space 72 (33) (2020), https://doi.org/10.1186/s40623-020-01158-6.
[27] P. Zingerle, R. Pail, T. Gruber, X. Oikonomidou, The combined global gravity field model XGM2019e, J. Geodes. 94 (7) (2020) 66, https://doi.org/10.1007/s00190-020-01398-0. Jul.
[28] C. Foerste, et al., EIGEN-6C4 the Latest Combined Global Gravity Field Model Including GOCE Data up to Degree and Order 2190 of GFZ Potsdam and GRGS Toulouse, 2014, https://doi.org/10.5880/icgem.2015.1.
[29] T.G. Farr, et al., The shuttle radar topography mission, Rev. Geophys. 45 (2007), https://doi.org/10.1007/3-540-44818-7_11.
[30] B. Tozer, D.T. Sandwell, W.H.F. Smith, C. Olson, J.R. Beale, P. Wessel, Global bathymetry and topography at 15 arc sec: SRTM15+, Earth Space Sci. 6 (10) (2019) 1847, https://doi.org/10.1029/2019EA000658, 1864, Oct.
[31] A. Zaki, A.H. Mansi, M. Selim, M. Rabah, G. El-Fiky, Comparison of satellite altimetric gravity and global geopotential models with shipborne gravity in the red sea, Mar. Geodes. 41 (3) (May 2018) 258–269, https://doi.org/10.1080/01490419.2017.1414088.
[32] R. Forsberg, A Study of Terrain Reductions, Density Anomalies and Geophysical Inversion Methods in Gravity Field Modelling, Ohio State University, 1984.
[33] Q. Liu, M. Schmidt, L. Sanchez, M. Willberg, Regional gravity field refinement for (quasi-) geoid determination based on spherical radial basis functions in Colorado, J. Geodes. 94 (10) (2020) 99, https://doi.org/10.1007/s00190-020-01431-2. Oct.
[34] Y. Liu, L. Lou, Unified land–ocean quasi-geoid computation from heterogeneous data sets based on radial basis functions, Rem. Sens. 14 (2013) 2022, https://doi.org/10.3390/rs14133015.
[35] A. Borghi, R. Barzaghi, O. Al-Bayari, S. Al Madani, Centimeter precision geoid model for jeddah region (Saudi arabia), Rem. Sens. 12 (12) (2020), https://doi.org/10.3390/rs12122066, 2066, Jun.
[36] I. Kalu, C.E. Ndehedehe, O. Okwuashi, A.E. Eyoh, Integration of satellite geodetic observations for regional geoid modeling using remove-compute-restore technique, Earth Sci. Inform. 15 (1) (Mar. 2022) 233–251, https://doi.org/10.1007/s12145-021-00716-0.
[37] O.C.D. Omang, R. Forsberg, How to handle topography in practical geoid determination: three examples, J. Geodes. 74 (6) (2000) 458–466, https://doi.org/10.1007/s001900000107.
[38] B. Heck, On Helmert's methods of condensation, J. Geodes. 77 (3–4) (Jun. 2003) 155–170, https://doi.org/10.1007/s00190-003-0318-5.
[39] W.E. Featherstone, M.C. Dentith, A Geodetic approach to gravity data reduction for geophysics, Comput. Geosci. 23 (10) (1998) 1063–1070.
[40] C. Jekeli, H.J. Yang, J.H. Kwon, Geoid determination in South Korea from a combination of terrestrial and airborne gravity anomaly data, J. Korean Soc. Surv. Geod. Photogramm. Cart. 31 (6_2) (Dec. 2013) 567–576, https://doi.org/10.7848/ksgpc.2013.31.6-2.567.
[41] R.J. Blakely, Potential Theory in Gravity and Magnetic Applications, Cambridge University Press, Cambridge, 1996.
[42] J.O. Ogundare, Introduction to least squares collocation and the kriging methods, in: Understanding Least Squares Estimation and Geomatics Data Analysis, Wiley, 2018, pp. 613–633.
[43] M.G. Sideris, Geoid determination by FFT techniques, in: F. Sansò, M. Sideris (Eds.), Geoid Determination, Lecture Notes in Earth System Sciences, 110, Springer, Berlin, Heidelberg, 2013, pp. 453–516.
[44] C. Hwang, Y.-S. Hsiao, Orthometric corrections from leveling, gravity, density and elevation data: a case study in Taiwan, J. Geodes. 77 (5–6) (Aug. 2003) 279–291, https://doi.org/10.1007/s00190-003-0325-6.

Rahayu Lestari is a graduate student in the department of Geodesy and Geomatics Engineering, Faculty of Earth Sciences and Technology, Institut Teknologi Bandung. Her research interest is geoid modeling.

Brian Bramanto is a researcher in Geodesy Research Group, Institut Teknologi Bandung (ITB). He received his master's degree in Geophysics (2018) from Institut Teknologi Bandung. His research involves in classical physical geodesy field and geodetic-based data analysis.

Kosasih Prijatna is an assistant professor in Faculty of Earth Sciences and Technology, Institut Teknologi Bandung. He has a doctoral degree in Geodesy from Institut Teknologi Bandung. His current research interests include physical geodesy and geodetic reference system.

Arisauna M. Pahlevi received Master degree in Geodesy and Geomatics Engineering from Bandung Institut Technology, Indonesia in 2016. She is currently serving as Mapping Surveyor at Geospatial Information Agency, Indonesia. Her area of interest focus on a vertical reference system, gravity, GNSS, and geoid data.

Widy Putra received master's degree in Geodesy and Geomatics Engineering from Bandung Institute of Technology (ITB) in 2021. He is currently working at Geospatial Information Agency, Indonesia. His research interests include gravity data processing and geoid modeling.

Raa Ina Sidrotul Munthaha is a Mapping Surveyor at Badan Informasi Geospasial (Geospatial Information Agency), Indonesia. His research concerns on geoid modelling using terrestrial and airborne gravity data.

Febriananda Ladivanov received Bachelor degree in Geodetic Engineering from Universitas Gadjah Mada in 2008. He is currently serving as Surveyor at Geospatial Information Agency, Indonesia. His area of interest includes the utilization of gravity, GNSS, and geoid data.